Journal of Power Sources 231 (2013) 146–152

Contents lists available at SciVerse ScienceDirect

Journal of Power Sources

journal homepage: www.elsevier.com/locate/jpowsour

Novel two-step processing route combining mechanical alloying and microwave hybrid sintering to fabricate dense $La_{9.33}Si_2Ge_4O_{26}$ for SOFCs

M. Santos [a], C. Alves [b], F.A.C. Oliveira [b], T. Marcelo [b], J. Mascarenhas [b], A. Cavaleiro [a], B. Trindade [a,*]

[a] CEMUC, Mechanical Engineering Department, University of Coimbra, Rua Luís Reis Santos, 3030-788 Coimbra, Portugal
[b] Laboratório Nacional de Energia e Geologia I.P., Estrada do Paço do Lumiar, 1649-038 Lisboa, Portugal

HIGHLIGHTS

- A novel processing route was used to fabricate $La_{9.33}Si_2Ge_4O_{26}$ for SOFCs.
- High density materials were obtained by microwave hybrid sintering.
- The sintered materials exhibit an apatite structure.
- Volatilization of germanium was prevented during sintering.

ARTICLE INFO

Article history:
Received 11 October 2012
Received in revised form
14 December 2012
Accepted 27 December 2012
Available online 5 January 2013

Keywords:
SOFC
Lanthanum-based oxyapatite
Mechanical alloying
Microwave hybrid sintering
Mechanical properties

ABSTRACT

In this work, microwave hybrid sintering at 1300 and 1350 °C was carried out for densification of $La_{9.33}Si_2Ge_4O_{26}$ mechanically alloyed powder with apatite structure. The pellets sintered at these two temperatures present the same structure (apatite) with relative densities of 92 and 96%, respectively. Mechanical analysis performed on sintered materials revealed the following results: hardness of 7.1 and 8.0 GPa, Young's modulus of 122 and 133 GPa, yield strength of 1807 and 2073 MPa and fracture toughness of 1.5 and 1.0 MPa $m^{1/2}$, respectively.

© 2013 Elsevier B.V. All rights reserved.

1. Introduction

Solid oxide fuel cells (SOFCs) are devices that allow direct conversion of chemical to electrical energy through an electrochemical reaction in a cleaner and more efficient way than conventional processes (e.g. gas turbines). The advantages of such cells include high-conversion efficiency, long-term stability, fuel flexibility and reduced emissions of polluting gases. However, it has proved difficult to develop this technology into commercially viable industrial products due to lack of appropriate electrolyte materials or manufacturing routes that would enable the cost of electricity per kW h to compete with existing technology. Yttria-stabilized zirconia (YSZ) has traditionally been used in electrolytes for SOFCs. This material exhibits high oxygen ion conductivity only at temperatures in the range of 850–1000 °C. Therefore, SOFCs using YSZ as an electrolyte must operate at similarly high temperatures, causing problems related to degradation of materials and mechanical and chemical compatibility in oxidizing and reducing atmospheres, cell sealing and life time. There is therefore a great deal of interest in lowering SOFC operation temperatures.

Recent research is being focused on the development of new materials for SOFC electrolytes with higher ionic conductivity at intermediate temperatures (500–800 °C) as alternative materials to YSZ. Rare earth silicates with an apatite-type structure, such as doped lanthanum oxides of general formula $La_{10}(MO_4)_6O_2$, where M = Ge, Co, Si, Al, or P, exhibit ionic conductivity higher than that of YSZ at intermediate temperatures, mainly due to the presence of oxide ion channels containing interstitial oxygen sites [1] combined with moderate thermal expansion coefficients and low electronic conductivities [2,3].

* Corresponding author. Tel.: +351 239790794.
E-mail addresses: bruno.trindade@dem.uc.pt, bruno.sacadura@gmail.com (B. Trindade).

0378-7753/$ – see front matter © 2013 Elsevier B.V. All rights reserved.
http://dx.doi.org/10.1016/j.jpowsour.2012.12.101

There are several references in the literature on the production of these materials by different routes, such as solid state reaction [2,4,5] wet-chemical techniques (sol–gel [6,7], alkoxide-hydrolysis [8], water-based gel-casting route [9], precipitation combined with an azeotropic distillation process [10], colloidal processing [11] floating zone methods [12]), hot pressing [13] or mechanical alloying with and without subsequent sintering [14–16], among others. Some attempts have also been made to produce these materials as tapes [17] or coatings [18,19].

The major limitation associated with the manufacturing of oxyapatite-based bulk materials is their poor sinterability. In order to make the electrolyte dense enough, apatite-type lanthanum silicates must be sintered at very high temperatures (1600 °C). Moreover, in the case of $La_{9.33}Si_2Ge_4O_{26}$ oxyapatite, very long heating at elevated temperatures leads to germanium volatilization and to the formation of insulating lanthanum-germanium oxides (e.g. La_2GeO_5) as the result of the increase of La/Ge atomic ratio [20]. Therefore, short sintering processes at relatively low temperatures are required in order to hinder volatilization of Ge above 1250 °C.

Mechanical alloying (MA) is recognized as a viable alternative for processing materials based on lanthanum oxides at sintering temperatures lower than those required by conventional routes. During MA the particles are subjected to strong deformation, increasing the density of defects, which enhances the densification process, due to decreasing of diffusion distances. In a recent work, dense oxyapatite-based $La_{9.33}Si_2Ge_4O_{26}$ materials have been successfully sintered by electrical heating at 1400 °C in static air from dry milled La_2O_3, SiO_2 and GeO_2 powders in a planetary ball mill [15]. EDS results showed that the content of germanium in the sintered materials remained almost constant, suggesting that once Ge is incorporated in the apatite phase, its volatilization is most likely prevented at temperatures up to 1400 °C.

The present work explores the possibility of densifying mechanically alloyed powders by microwave (MW) sintering with the assistance of susceptors of silicon carbide (hybrid heating), at temperatures considerably lower than the ones used in conventional solid state sintering (typically 1600 °C). Lower sintering temperatures and shorter dwell times not only will reduce the cost involved in the processing but also might help to reduce both the volatilization of Ge and the formation of undesirable secondary phase oxides with reduced ionic conductivity. The effect of two sintering temperatures (1300 and 1350 °C) on the density, structure and mechanical properties of $La_{9.33}Si_2Ge_4O_{26}$ pellets densified by microwave hybrid sintering from MA powders will be presented and discussed.

2. Experimental

$La_{9.33}Si_2Ge_4O_{26}$ powder was obtained from a mixture of La_2O_3 (99.9%), SiO_2 (99.4%) and GeO_2 (99.9%) powders from Neyco by mechanical alloying (MA) in a Fritsch planetary ball mill. The constituent powders were placed in a 250 ml hardened steel vial together with 20 mm diameter balls made with the same material, keeping a ball-to-powder weight ratio of 20:1. Dry mechanical milling was carried out in a protective atmosphere (argon at 200 kPa) by using a rotating speed of 350 rpm for 15 h. Prior to the synthesis of $La_{9.33}Si_2Ge_4O_{26}$, the starting materials were milled separately at 350 rpm for 30 min in argon at 50 kPa in order to achieve fine particle sizes with a greater ability for sintering. After mechanical alloying, particle size distribution of the $La_{9.33}Si_2Ge_4O_{26}$ was measured by laser scattering (CILAS 1064) from a powder suspension in water under mechanical agitation after a 60 s sonication. Scanning electron microscopy with electron dispersive spectrometry (SEM/EDS Philips XL30FEG/EDAX) was used for characterization of the MA particles morphology. X-ray diffraction (XRD) analysis was performed for phase evaluation in a Philips X'Pert PW 3020 equipment. The measurements were performed using CoK_α ($\lambda = 1.78897$ Å) within the 2θ range of 20–60° using a step size of 0.04° (2θ) and an acquisition time of 3 s per step. Phase identification was carried out with reference to the ICDD database.

The MA powder was compacted by uniaxial pressing at 390 MPa followed by microwave sintering for 1 h at temperatures of 1300 and 1350 °C (hereafter referred to as materials S1 and S2, respectively) under static air in a Microwave Research Applications Inc. furnace with a 2.45 GHz frequency and a nominal power of 1 kW. Temperature was controlled by using an S-type thermocouple (Pt–Pt10%Rh) placed near the samples. The geometric density (weight/volume) of the green compacted samples was measured. For the sintered samples, density and open porosity were determined using the boiling test method. SEM/EDS, XRD and atomic force microscopy (AFM) were also used for samples characterization. SEM/EDS observations were carried out on polished cross sections, coated with a thin layer of Au–Pd or Cr to provide surface electrical conductivity (Sputter Coater Emitech K575X). The samples were transversely fractured and the surfaces analyzed by SEM/EDS. Concerning AFM analysis, a Kruger Innova microscope, capable of performing scans up to 90 μm was used. The scans were performed using an MPP-12 Cantilever and an MPP-12200-10 Probe with 150 kHz resonance frequency and a constant force of 5 N m^{-1}. Scans were obtained by intermittent contact, known as tapping mode. A modular multiplatform software for profilometric data analysis, Gwyddion v2.28 [21] was used for image analysis.

Nanoindentation tests were performed on the polished surfaces using a NanoTest Platform from MicroMaterials, equipped with a Berkovich indenter. Corrections of the geometrical imperfections of the tip indenter, thermal drift of the equipment and zero indentation-depth position were performed. A set of indentations at different loads (from 10 mN to 100 mN) were performed and used for the determination of nanohardness (H) and Young's Modulus (E) according to the depth sensing indentation method described elsewhere [22]. Two creep periods of 30 s were programmed during tests in order to stabilize the penetration depth before unloading, for thermal drift correction. In order to obtain representative average values for the evaluated properties, 100 indentation tests were performed on each material.

A Shimadzu indentation equipment with a Vickers diamond indenter was used for the determination of Vickers hardness (HV1), fracture toughness (K_c) and yield stress (σ_y).

This technique was used to perform measurement at loads higher than 100 mN and the HV1 values were converted in GPa for comparison with the hardness measured by the depth sensing indentation technique. Three loads (200, 300 and 500 mN) were applied in order to analyze the indentation size effect (ISE) contribution. The nanoindentation results were also used for this analysis.

The fracture toughness (K_c) of the materials was determined by the indentation fracture method [23]. A 4.9 N load was chosen to assure the appearance of cracks at the corners of the indentations. Ten measurements from randomly selected areas of each material were performed, according to the ASTM standard [24]. The total crack lengths emanating from the Vickers indentation fracture tests were measured by AFM.

Finally, yield stress (σ_y) was determined from the results of the indentation tests by means of the reverse analysis approach proposed by Antunes et al. [25].

3. Results and discussion

3.1. Mechanical alloying

Fig. 1 shows the particle size distribution (differential and cumulative curves) obtained from the MA powder. The size distribution is

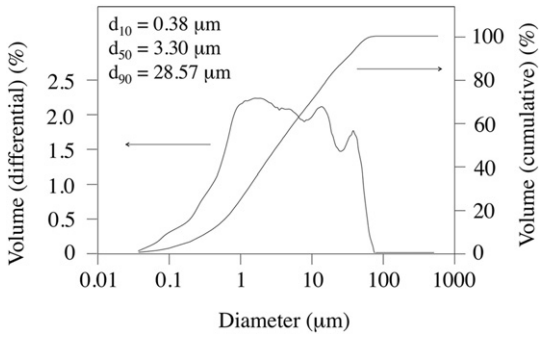

Fig. 1. Particle size distribution of the MA powder.

multimodal and quite large with characteristic particle diameters d_{10}, d_{50} and d_{90} of 0.38, 3.30 and 28.57 μm, respectively.

Microstructural characterization by SEM of MA particles is shown in Fig. 2. It can be seen that the resulting particles consist of agglomerates of smaller particles, some of which are nanosized. This is typical of the MA process in which repeated cold welding, fracturing and re-welding of powders occur, giving rise to new particles with different compositions up to the synthesis is completed and homogeneous composition is obtained.

XRD pattern of the MA powder is shown in Fig. 3. As expected on the basis of previous work [15] the diffraction peaks correspond to a nanometric apatite phase. The lattice parameters of the apatite $La_{9.33}Si_2Ge_4O_{26}$ formed during milling are the following: $a = 9.91$ Å and $c = 7.26$ Å. No ICDD card is available for the composition $La_{9.33}Si_2Ge_4O_{26}$. However, taking into account the two cards published in the literature for $La_{9.33}Si_6O_{26}$ (ICDD card no. 49-0443) and $La_{9.36}Si_3Ge_3O_{26}$ (ICDD card no. 75-3458), the diffraction peaks position of apatite formed during MA match better to Ge-doped apatite. In fact, when compared to the ICDD card of apatite with no germanium, the diffraction peaks of apatite $La_{9.33}Si_2Ge_4O_{26}$ are shifted to lower angles (higher interplanar distances) as a result of the larger size of the Ge atom when compared to the Si one (ionic radius of 0.67 Å for Ge^{4+} and 0.54 Å for Si^{4+}).

In addition to the apatite diffraction peaks, a trace of another phase (main peak at $2\theta \sim 33°$) is also evident in Fig. 3, suggesting that the reaction was not fully completed. Indeed, it is likely that this phase is the lanthanum oxide, La_2O_3.

3.2. Sintering behavior

The green density of the compacts as well as the bulk densities of the samples sintered for 1 h at 1300 and 1350 °C under static air

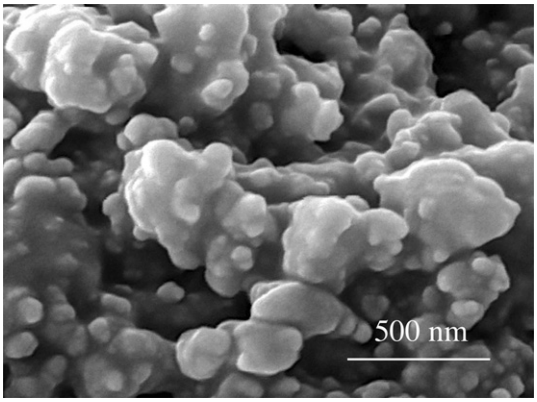

Fig. 2. SEM micrograph of particles of the MA powder.

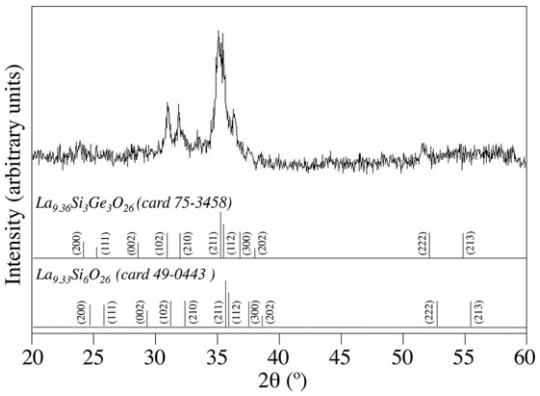

Fig. 3. X-ray diffraction pattern of the MA powder.

in a microwave furnace, together with the open porosities of the pellets, are presented in Table 1.

Material S2 sintered at 1350 °C showed higher density and, consequently, lower porosity than S1 sintered at 1300 °C. These materials are denser than the ones obtained in a previous work [15], sintered in an electric furnace at the same temperatures (5.04 against 4.81 g cm^{-3} at 1300 °C and 5.25 against 5.13 g cm^{-3} at 1350 °C).

In a conventional furnace, radiation is the dominant heat transfer mechanism over conduction and convection at temperatures above 700 °C, while in a microwave furnace the electromagnetic field power is converted into heat within the material. In this work, susceptors of silicon carbide were used, since this material absorbs MW radiation from room temperature. This allows heating the samples up to the temperature at which they start to absorb the radiation. This process is referred in the literature as hybrid heating. It relies on microwave heating by the electromagnetic field, which has some advantages over conventional heating, such as much higher heating rates and shorter sintering cycles (about 3.5 h when compared to 12 h in a conventional furnace). This is a very important aspect in particular for Ge-doped apatites, since shorter times at high temperatures may contribute for minimizing GeO_2 volatilization occurring at temperatures above 1250 °C.

Taking into account the results already published [15] and the ones of this work on microwave hybrid sintering, a linear trend between the sintered density and the open porosity is clearly observed, as shown in Fig. 4. Based on this correlation, a value of 5.45 g cm^{-3} is estimated for fully dense $La_{9.33}Si_2Ge_4O_{26}$ materials. This value is similar to the one reported for the apatite $La_{9.36}Si_3Ge_3O_{26}$ (5.48 g cm^{-3}, from ICDD card no. 75-3458). However, it should be noted that the density value of the voids-free $La_{9.33}Si_2Ge_4O_{26}$ material is just an estimation obtained by a linear trend from samples with different levels of porosity. Considering this reference value, materials S1 and S2 present relative densities close to 92 and 96%, at 1300 °C and 1350 °C, respectively. This implies that material S2 contains about 1% of closed porosity whereas S1 only contains open porosity.

Fig. 5a–d shows AFM images of the sintered materials S1 (a, b) and S2 (c, d). Fig. 5b and d corresponds to thermal etched materials. This treatment was performed 50 °C below the sintering temperatures during 10 min (1250 °C for S1, 1300 °C for S2). Material S2

Table 1
Green and sintered density of the pellets and open porosity measured on sintered pellets.

Sample identification	Green density (g cm^{-3})	Bulk density (g cm^{-3})	Open porosity (%)
S1	3.6	5.0	8.3
S2	3.6	5.3	3.4

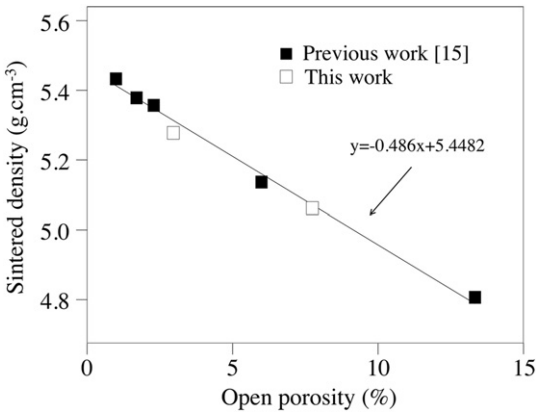

Fig. 4. Relationship between open porosity and sintered density for the sintered $La_{9.33}Si_2Ge_4O_{26}$ pellets.

presents fewer pores than S1 confirming the results obtained for both bulk density and open porosity. In both cases, the pores are typically smaller than 5 μm (mean equivalent diameter of 3.2 and 2.5 μm was determined by image analysis from materials S1 and S2, respectively) and are mostly round and of closed type indicating that the sintering stage was close to full densification. Another important feature to notice is the difference in the grain size of the two materials. A difference of 50 °C in the sintering temperature was responsible for a significant increase of grain size. Average values of 0.7 and 1.1 μm (Fig. 5b and d) were determined for samples S1 and S2, respectively. Grain coarsening can be due to both grain boundary motion and Ostwald ripening mechanisms, since diffusion is faster at higher temperatures; it can also be due to non-thermal effect of MW radiation [26].

The XRD patterns of the microwave hybrid sintered materials are shown in Fig. 6. The two sintered temperatures used in this work do not seem to have a clear effect on the phases formed, the apatite-type structure being the major phase in both materials.

The calculated lattice parameters, *a* and *c*, of both sintered materials (9.84 and 7.25 Å, respectively) are slightly lower than the ones calculated from the milled mixture, the values tending to reach the ones indicated for the $La_{9.36}Si_3Ge_3O_{26}$ phase (ICDD card 75-3458). Besides, two peaks in the 2θ range 30–35° were also detected and ascribed to the phase La_4GeO_8 (ICDD card 040-1185). This phase was also observed in a previous work [15] for conventional sintered $La_{9.33}Si_2Ge_4O_{26}$ pellets and might be due to a non-homogeneous distribution of Si in the MA powder.

EDS analysis performed on different areas of these two materials did not reveal any differences in chemical composition. Fig. 7 shows an EDS spectrum characteristic of both materials. The element Ge was detected in the same quantity in the samples before and after sintering (not shown) confirming that volatilization of this element was prevented by the sintering method/cycle used in this work. However, both materials experienced a mass loss of around 5%. TG analysis revealed that the mass loss occurred up to 600 °C, which cannot be attributed to the volatilization of germanium but to a deficient drying of the mechanical alloying mixture or even to the presence of residual unreacted phases such as La_2O_3. This oxide is very reactive with water and carbon dioxide from the ambient atmosphere giving rise to the formation of $La(OH)_3$ and $La_2(OH)_4CO_3 \cdot nH_2O$. According to the literature, these phases decompose upon heating in the range 280–600 °C, with significant weight loss of the samples (up to 63.5% of the total weight loss at 280 °C) [27].

Sansom et al. [28] have shown that for $La_{9.33}Si_2Ge_4O_{26}$ pellets heated at 1500 °C for 5 days a weight loss of 2% was recorded and the X-ray pattern of the apatite phase appeared unchanged. These authors reported formation of the insulating phase La_2GeO_5 during sintering. Therefore, the volatilization of Ge at temperatures up to 1350 °C can be ruled out in the present work, based on the experimental evidence.

3.3. Mechanical properties

Indentation size effect (ISE) was analyzed for both materials (Fig. 8). ISE denotes the general tendency for hardness to vary with load and this is especially apparent in the case of hard and brittle ceramics.

As expected, hardness of both materials increased with decreasing load. This is especially noticeable for lower indentation loads (nanoindentation tests) where no fracture occurred at the corners of the indentations. Local cracking can affect both depth and size of the indentation, since part of the transferred energy to the material surface is spent in the initiation and propagation of the cracks rather than in the indentation process.

For loads higher than 100 mN, there is a clear separation of the two curves, this phenomenon being more evident for higher

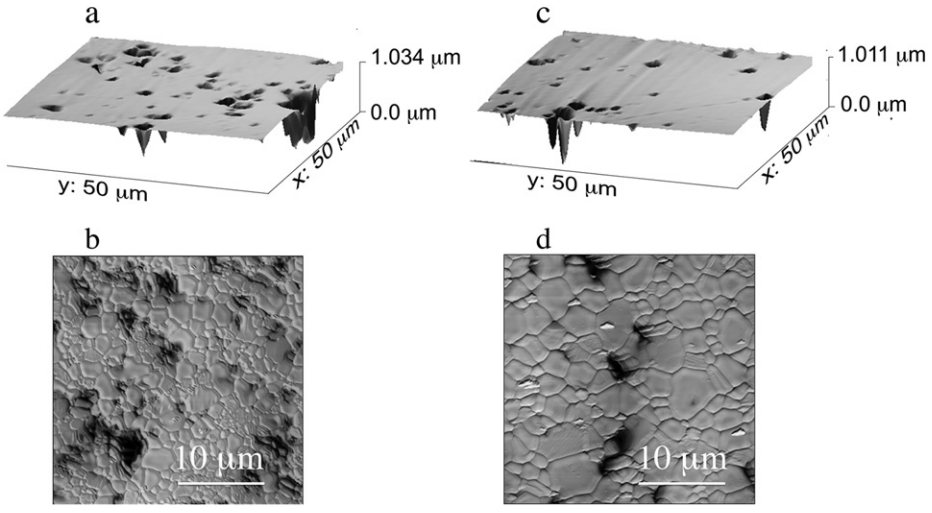

Fig. 5. AFM micrographs of the surfaces of the sintered materials S1 (a, b) and S2 (c, d).

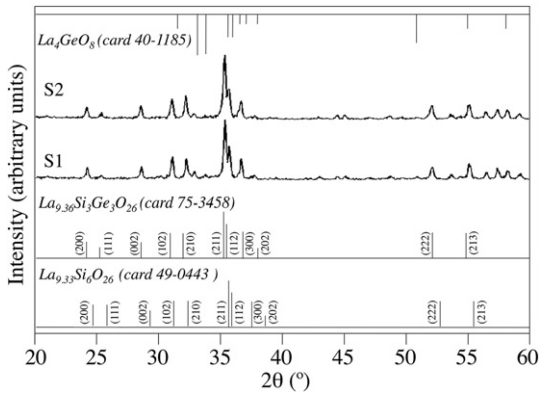

Fig. 6. X-ray diffraction patterns of the sintered S1 and S2 materials.

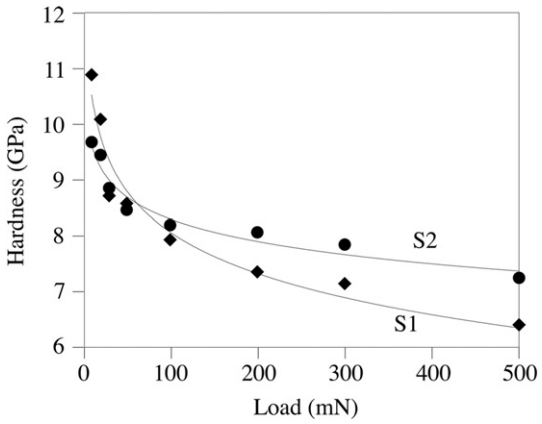

Fig. 8. Influence of applied load on the hardness of the sintered materials S1 and S2.

applied loads. This is attributed to the microporosity of the materials. Indeed, material S1 is more porous than S2 (8% against 3%) and, therefore, its hardness is more influenced by porosity at higher applied loads.

The hardness at infinite depth (H_0) of materials was determined using the Nix and Gao model [29]. Accordingly, H_0 can be derived from the following equation:

$$H^2 = H_0^2\left(1+\frac{h^*}{h}\right) \quad (1)$$

where H is the hardness for a given depth of indentation, h (nm), H_0 (GPa) is the hardness at the limit of infinite depth and h^* (nm) is a characteristic length that depends on the shape of the indenter, the shear modulus and H_0. H_0 can be therefore obtained from a H^2 versus $1/h$ plot for $1/h = 0$. Fig. 9 is a representation of H^2 versus $1/h$ for materials S1 and S2.

A reasonable good linear relationship is obtained for both materials (correlation coefficient R^2 of 0.96 and 0.95), suggesting that the present data fits well the micro hardness-depth Nix-Gao model (eq. (1)), even for the highest applied load. For $1/h = 0$, H_0 values of 7.1 and 8.0 GPa are obtained for materials S1 and S2, respectively. These values are consistent with the ones obtained for conventionally sintered materials [30]. It should be noticed that the maximal loads applied in the two studies were different (1000 mN in the previous study against 500 mN in the present study) which explains the slightly higher hardness values recorded in the present work.

The Young's modulus, E, was calculated from nanoindentation tests with different applied loads, from 10 to 100 mN. Mean values of 123 and 133 GPa were obtained for materials S1 and S2, respectively. As expected, Young's modulus decreased when the porosity increased as observed by Giraud and Canel [31] for different porous ceramic materials. The values achieved are in good agreement with those reported in the literature [30,32].

As mentioned in the Experimental section, fracture toughness of the sintered materials was determined from indentation tests with a 4.9 N load. This load was chosen to assure the formation of cracks at the indentation corners (Fig. 10). In order to define the crack formation model, the indented samples were progressively polished and different layers at different depths were observed by optical microscopy. The cracks nucleate at the tip of the indenter and propagate into the underlying material. They were classified as median cracks and the K_c was determined according to the JIS R 1607 standard [33] from direct measurements of the crack traces on indented surfaces, by the following equation:

$$K_c = 0.018\left(\frac{E}{H}\right)^{1/2}\left(\frac{P}{c^{3/2}}\right) \quad (2)$$

where: E is the Young modulus, H is the Vickers hardness, P is the indentation load and c is half of average of the crack length. Values of 1.5 ± 0.33 and 1 ± 0.14 MPa $m^{1/2}$ (characteristic of very brittle materials) were obtained for materials S1 and S2, respectively. Although the difference is not significant, the higher K_c value is associated to the more porous material (S1), presenting the lower values of hardness and Young's modulus. It is well known that crack

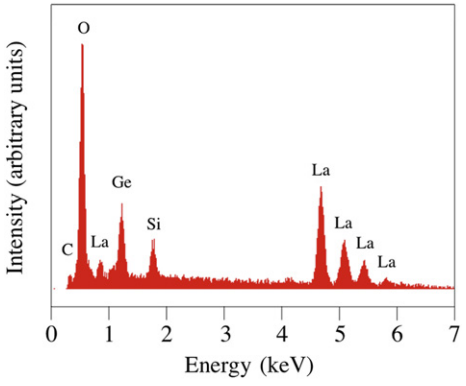

Fig. 7. Typical EDS spectrum representative of both materials.

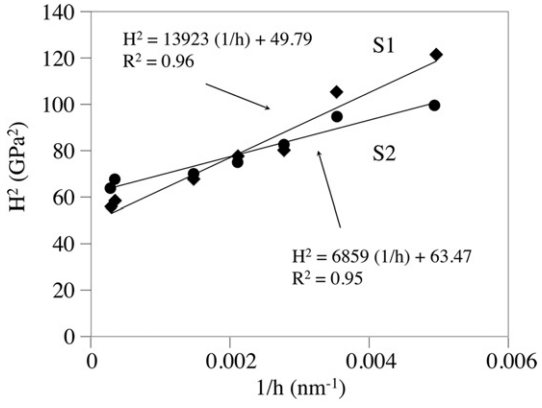

Fig. 9. H^2 versus $1/h$ from the sintered materials S1 and S2 (hardness results).

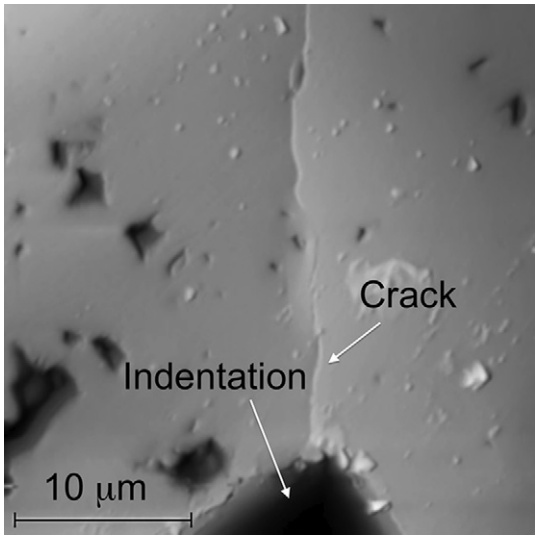

Fig. 10. Crack at the corner of a Vickers indentation ($P = 4.9$ N).

path propagation is affected by the porosity which absorbs part of the fracture energy.

According to the literature [34], higher values of K_c are expected for less-porous materials, which is not in accordance with the values obtained in the present work. This might be explained by the increased grain size occurred for $T = 1350$ °C, and the fact that the sample S2 is harder than sample S1. In addition, eventual errors related to determining the length of the cracks may affect the final value of fracture toughness.

In order to better define the mechanical behavior of the materials, two reverse analysis methodologies [25,35] were employed for the calculation of the yield stress σ_y and the representative stress, σ_r from the experimental micro-indentation results. Both approaches are based on the assumption that materials with the same reduced elastic modulus, E^*, and σ_r exhibit similar behavior under loading indentation, whatever the value of the strain-hardening exponent, n.

The reverse analysis approach proposed by Antunes et al. [25] directly compares experimental to numerical simulation indentation results. This reverse analysis methodology extracts σ_r, by comparing the loading part of the experimental and numerical indentation curves. In the case of the reverse analysis approach proposed by Dao et al. [35], an analytical method is used to determine σ_r (corresponding to a plastic strain value ε_r of 3.3%).

Table 2 summarizes σ_y and σ_r values calculated for the sintered materials. For comparison, the values obtained for materials with the same chemical composition sintered in a conventional electric furnace are also presented. As observed for hardness and Young's modulus, the increase in the sintering temperature from 1300 to 1350 °C is responsible for higher yield stress values. These values are significantly higher than the ones obtained for materials with the same chemical composition, sintered at the same temperature by conventional sintering [30]. This can be explained by the higher density of the materials produced by microwave sintering.

Taking into account the results obtained in this work, it is evident that some adjustments must be done to the sintering process. Shorter MW hybrid sintering cycles are envisaged in order to produce materials with small grain sizes and to prevent formation of undesirable phases at high temperatures. Moreover, ionic conductivity tests will be carried out in order to evaluate the ability of these materials to be used as oxide ion conducting electrolytes for SOFCs.

Table 2
σ_y and σ_r values of the materials obtained by two distinct methods. Values obtained in previous work from conventionally sintered materials are also presented for comparison.

Sample	Antunes et al. [25]		Dao et al. [35]	
	σ_y (MPa)	σ_r (MPa)	σ_y (MPa)	σ_r (MPa)
S1 ($T = 1300$ °C)	1807	2009	1790	1874
S2 ($T = 1350$ °C)	2073	2305	2058	2154
Conventional sintering $T = 1300$ °C [30]	779	812	771	804
Conventional sintering $T = 1350$ °C [30]	1169	1219	1185	1235

4. Conclusions

In this work, microwave hybrid sintering was successfully used for densification of mechanically alloyed $La_{9.33}Si_2Ge_4O_{26}$ powder at temperatures of 1300 and 1350 °C. The results showed that the combination of these techniques (MA and MW) allows obtention of high density materials with apatite structure. The samples sintered at those two temperatures present relative densities of 92 and 96%, respectively. The mechanical properties showed a direct dependence on the sintering temperature. Samples sintered at 1350 °C presented the higher values of hardness (8.0 against 7.1 GPa), Young's modulus (133 against 122 GPa) and yield strength (2073 against 1807 MPa), respectively. Low fracture toughness values were obtained for both materials, 1.5 and 1.0 MPa $m^{-1/2}$, for samples S1 and S2, respectively.

Acknowledgments

This research is partially sponsored by FEDER funds through the program COMPETE – Programa Operacional Factores de Competitividade – and by national funds through FCT – Fundação para a Ciência e Tecnologia – under the contract PTDC/EME-PME/102837/2008. The research fellowships granted to Cátia Alves and Márcio Santos are also gratefully acknowledged.

References

[1] L. Leon-Reina, E. Losilla, M. Martinez-Lara, S. Bruque, M. Aranda, J. Mater. Chem. 14 (2004) 1142–1149.
[2] Y. Higuchi, M. Sugawara, K. Onishi, M. Sakamoto, S. Nakayama, Ceram. Int. 36 (2010) 955–959.
[3] D. Marrero-Lopez, M.C. Martin-Sedeno, J. Pena-Martinez, J.C. Ruiz-Morales, P. Nunez, M.A.G. Aranda, J.R. Ramos-Barrado, J. Power Sources 195 (2010) 2496–2506.
[4] A. Shaula, V. Kharton, J. Waerenborgh, D. Rojas, F. Marques, J. Eur. Ceram. Soc. (2005) 2583–2586.
[5] K. Fukuda, T. Asaka, N. Ishizawa, H. Mino, D. Urushihara, A. Berghout, E. Béchade, O. Masson, I. Julien, P. Thomas, Chem. Mater. 24 (2012) 2611–2618.
[6] E. Jothinathan, K. Vanmeensel, J. Vleugels, O. Van der Biest, J. Alloys Compd. 495 (2010) 552–555.
[7] J. Zhou, X.F. Ye, J.L. Li, S.R. Wang, T.L. Wen, Solid State Ionics 201 (2011) 81–86.
[8] Y. Masubuchi, M. Higuchi, T. Takeda, S. Kikkawa, J. Alloys Compd. 408–412 (2006) 641–644.
[9] S.P. Jiang, L. Zhang, H.Q. He, R.K. Yap, Y. Xiang, J. Power Sources 189 (2009) 972–981.
[10] H.-C. Yao, J.-S. Wang, D.-G. Hu, J.-F. Li, X.-R. Lu, Z.-J. Li, Solid State Ionics 181 (2010) 41–47.
[11] I. Santacruz, J.M. Porras-Vazquez, E.R. Losilla, M.A.G. Aranda, J. Eur. Ceram. Soc. 31 (2011) 1573–1580.
[12] S. Nakayama, M. Sakamoto, M. Higuchi, K. Kodaira, M. Sato, S. Kakita, T. Suzuki, K. Itoh, J. Eur. Ceram. Soc. 19 (1999) 507–510.
[13] P.J. Panteix, I. Julien, P. Abelard, D. Bernache-Assollant, Ceram. Int. 34 (2008) 1579–1586.

[14] M.M. Vieira, J.C. Oliveira, A. Cavaleiro, B. Trindade, Rev. Adv. Mater. Sci. (2008) 344–348.
[15] R. Serra, C. Alves, F.A.C. Oliveira, T. Marcelo, J. Mascarenhas, B. Trindade, Ceram. Int. 38 (2012) 5355–5361.
[16] L.G. Martinez-Gonzalez, E. Rodriguez-Reyna, K.J. Moreno, J.I. Escalante-Garcia, A.F. Fuentes, J. Alloys Compd. 476 (2009) 710–714.
[17] C. Bonhomme, S. Beaudet-Savignat, T. Chartier, C. Pirovano, R.-N. Vannier, Mater. Res. Bull. 45 (2010) 491–498.
[18] M.M. Vieira, J. Oliveira, A.L. Shaula, A. Cavaleiro, B. Trindade, Surf. Coat. Technol. 206 (2012) 3316–3322.
[19] W. Gao, H.-L. Liao, C. Coddet, J. Power Sources 179 (2008) 739–744.
[20] L. Leon-Reina, M. Martin-Sedeno, E. Losilla, A. Cabeza, M. Martinez-Lara, S. Bruque, E.R. Losilla, A. Cabeza, M. Martinez-Lara, S. Bruque, F.M.B. Marques, D.V. Sheptyakov, M.A.G. Aranda, Chem. Mater. 15 (2003) 2099–2108.
[21] P. Klapetek, D. Necas, C. Anderson, Gwyddion v2.24 (Software package) (2010), http://gwyddion.net/.
[22] A. Sakly, J. Costa, B. Trindade, J.V. Fernandes, T. Benameur, J. Alloys Compd. 502 (2010) 480–487.
[23] R. Spiegler, S. Schmadder, J. Hard Mater. 1 (1990) 147–158.
[24] ASTM E384-99 Standard Test Method for Microindentation Hardness of Materials, ASTM International, West Conshohocken, PA, USA, 1999.
[25] J.M. Antunes, J.V. Fernandes, L.F. Menezes, B.M. Chaparro, Acta Mater. 55 (2007) 69–81.
[26] Z. Jiao, N. Shikazono, N. Kasagi, J. Power Sources 195 (2010) 8019–8027.
[27] J.P. Panteix, I. Julien, D. Bernache-Assollant, P. Abelard, Mater. Chem. Phys. 95 (2006) 313–320.
[28] J. Sansom, A. Najib, P.R. Slater, Solid State Ionics 175 (2004) 353–355.
[29] W. Nix, H. Gao, J. Mech. Phys. Solids 46 (1998) 411–425.
[30] M. Santos, C. Alves, F.A.C. Oliveira, T. Marcelo, J. Mascarenhas, J.V. Fernandes, B. Trindade, Ceram. Int. 38 (2012) 6151–6156.
[31] S. Giraud, J. Canel, J. Eur. Ceram. Soc. 28 (2008) 77–83.
[32] P. Vullo, M. Davis, J. Non-Cryst. Solids (2004) 180–184.
[33] JIS R 1607, Japanese Industrial Standard, Testing Methods for Fracture Toughness of High Performance Ceramics, 1990.
[34] M. Zheng, X. Zheng, Z.J. Luo, Int. J. Fracture 58 (1992) 51–55.
[35] M. Dao, N. Chollacoop, K. Van Vliet, T. Venkatesh, Acta Mater. 19 (2001) 3899–3918.